Numerical prediction of grain structure formation during laser powder bed fusion of 316 L stainless steel

Anaïs Baumard, Danièle Ayrault, Olivier Fandeur, Cyril Bordreuil, Frédéric Deschaux-Beaume

Materials and Design 199 (2021) 109434

Contents lists available at ScienceDirect

Materials and Design

journal homepage: www.elsevier.com/locate/matdes

Numerical prediction of grain structure formation during laser powder bed fusion of 316 L stainless steel

Anaïs Baumard [a,*], Danièle Ayrault [a], Olivier Fandeur [a], Cyril Bordreuil [b], Frédéric Deschaux-Beaume [b]

[a] Université Paris-Saclay, CEA, Service d'Etudes Mécaniques et Thermiques (SEMT), 91191 Gif-sur-Yvette, France
[b] LMGC, Univ. Montpellier, CNRS, Montpellier, France

HIGHLIGHTS

- Manufacturing of single lines on an instrumented test bench at velocities similar to those reached during the LBM process.
- Comparison of the grain structure resulting from "CAFE" simulations to the experimental one.
- The resulting grain structure is directly dependent on the growth model defined in the solidification algorithm.
- The laser power and velocity strongly influence the thermal gradient and cooling rate, leading to variation of grain characteristic.

GRAPHICAL ABSTRACT

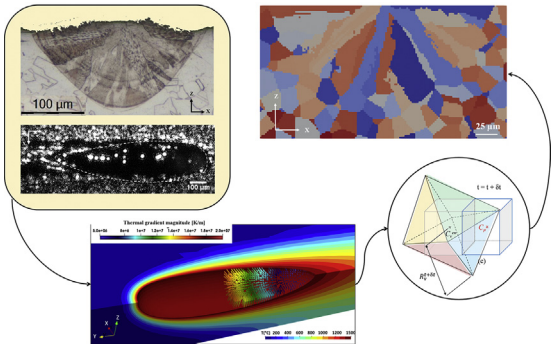

ARTICLE INFO

Article history:
Received 4 November 2020
Received in revised form 9 December 2020
Accepted 20 December 2020
Available online 25 December 2020

Keywords:
Additive manufacturing
Laser powder bed fusion (LPBF)
CAFE model
316 L stainless steel
Grain structure prediction

ABSTRACT

Additive Manufacturing (AM) processes enable the reduction of manufacturing time, material waste, and allows for the creation of complex structures. However, anisotropic mechanical behaviour is frequently observed in additively manufactured parts, and it is directly linked to the component's grain structure characteristics, which itself is dependent on the process parameters. The formation of grain structure in 316 L stainless steel fusion lines is investigated in this paper, combining experimental results and numerical simulations. Experimentally, fusion lines are built on a 316 L substrate, using an instrumented LPBF process. The high-speed camera recordings combined with the characterization of the samples enables capturing of melt-pool sizes and grain characteristics. The numerical modelling is based on a three-dimensional "CAFE" model, coupling Cellular Automata and Finite Element models to predict grain formation. The thermal model is defined and calibrated using the experiments. The experimental and numerical grain characteristics are compared. Numerical results are discussed with regards to the growth models and the process parameters. The growth model defined here is compared to existing models and is well fitted to capture grain formation in single-track configurations. Finally, the average grain size and aspect ratio of the grains increase with an increase of the process' linear energy.

1. Introduction

Interest in metal Additive Manufacturing (AM) has risen in recent years [1]. It is now used in diverse domains and applications, ranging from medical applications [2] to aerospace component fabrication [3]. The main advantage of AM is the ability to design parts with low

* Corresponding author.
E-mail addresses: anais.baumard@cea.fr (A. Baumard), danielle.ayrault@cea.fr (D. Ayrault), olivier.fandeur@cea.fr (O. Fandeur), cyril.bordreuil@umontpellier.fr (C. Bordreuil), frederic.deschaux-beaume@umontpellier.fr (F. Deschaux-Beaume).

https://doi.org/10.1016/j.matdes.2020.109434

porosity and complex geometries that would be impossible to obtain by conventional processes and typical tooling.

Laser Powder Bed Fusion (LPBF), also known as Selective Laser Melting (SLM) is a metal AM process which enables the creation of three-dimensional parts using powder bed technology [4]. A thin layer of metallic powder is deposited onto a plate in a building chamber and locally melted by a laser beam. The building platform then goes down and a new layer of powder is left. This cycle is repeated as many times as required for the building of the part.

The microstructures of the materials produced by LPBF are strongly dependent on the mechanisms that take place during the solidification of the molten powder. The high energy density of the laser, combined with the fast displacement of the heat source, create specific thermal histories in the material, which tends to produce columnar grain structures [5–9]. However, the grain shape and size are strongly influenced by the manufacturing parameters. The laser's characteristics (power, scanning speed, wavelength), the building strategy (hatching distance, inter-layer rotation) as well as the machine conditions (initial temperature, gas composition) are some relevant manufacturing parameters. Many research papers have been conducted recently on the influence of building parameters on microstructures [10–14].

In stainless steel components, the mechanical properties of the parts depend primarily on the chemical composition of the material and its grain structure. Many researchers have investigated mechanical properties in parts obtained by LPBF [11,13,15–17]. These studies highlighted the anisotropic mechanical behaviour of the produced components, which largely correlated to a component's columnar grain structure. This can be a major issue if the spatial variation of the samples' mechanical properties depends on its orientation on the building platform, as investigated for instance by Kunze et al. [18]. These authors have shown that cylindrical samples of IN738 have a 30% lower Young modulus when their cylinder axis is parallel to the building direction (BD), than when its axis is perpendicular to this direction. However, if controlled, anisotropic mechanical behaviour is not necessarily an encumbrance and can be compatible with eventual material and/or design requirements. This is discussed in two studies conducted by Y. Yang et al. on the wear behaviour of a laser melted 316 L sample, revealing that the columnar aspect of the grain's structure increases the wear resistance of the part when the sliding direction is perpendicular to the columnar structure [19,20]. Consequently, it is crucial to understand the correlation between grain formation and the process parameters.

Recent studies developed numerical models in order to predict the grain structure formation during LPBF process [21,22]. These studies are based on the cellular automata (CA) method initially developed by John von Neumann in 1948 [23], and later applied by Gandin et al. to model the grain structure formation in solidification processes [24,25]. In order to predict grain formation, CA modelling must be coupled with a thermal model of the process, which calculates the thermal fields and histories that control grain growth. Various methods have been investigated to couple with CA: the Finite Volume method [26–30], Finite Differences method, [21,31], or analytical heat source modelling [32]. These studies focused on the CA results, and only little attention was paid to the validation of the thermal fields, which are essentially considered as input data for the grain growth simulation. However, these thermal fields governing the growth conditions during solidification, have to be as realistic as possible to predict representative grain structures. In particular, the melt pool simulated should be of realistic size and shape. The numerical grain structure also depends on the growth's kinetic law introduced in the model. As a general rule, a power law connecting the grain growth speed and the undercooling is used. For given cooling conditions and a material, the law parameters are identified using the undercooling expression proposed by Kurz et al. [33,34]. However, the identification of these model's parameters is rarely detailed, and the various growth kinetic laws identified in the literature for some materials are not compared to discuss their differences and effect on the modelled grain structure.

The objective of this work is to implement a grain growth prediction model in order to study the effect of the process parameters on grain formation during LPBF. For that purpose, two models are developed: a thermal Finite Elements (FE) model to simulate the thermal effects induced by the process, and a grain growth model based on Cellular Automata (CA). These two models are coupled using the "CAFE" method initially developed by Gandin et al [25]. An experimental study carried out on an instrumented LPBF device was also conducted, where fusion lines were carried out on a 316 L stainless steel substrate with various process parameters. This part is important as it allows for the calibration of the heat source model employed, leading to a numerical melt pool with an appropriate size and geometry. The numerical results concerning the modelling of fusion lines were compared to experimental results. The influence of the growth's kinetic model and of some process parameters on the characteristics of the predicted grain structures are also discussed.

2. Experimental procedure

2.1. LPBF equipment

The laser powder bed fusion test bench of the Processes and Engineering in Mechanics and Materials (PIMM - ENSAM) laboratory was used. The bench is shown in Fig. 1 and is equipped with:

- a high-speed table ($v_{max} = 1\ ms^{-1}$) on which a plate is fixed as a substrate for the fusion lines;
- a TRUMPF® continuous wave Ytterbium-YAG laser operating at a wavelength of 1030 nm, with a focal spot size of 150 μm;
- a CAVILUX® lighting laser operating at 810 nm;
- a Photron UX100® high-speed camera equipped with 2 filters to detect only reflected light from the lighting laser;
- an airtight box fixed on the table, filled with argon to reduce oxygen content (less than 1000 ppm). On the top of the box, several quartz panes allow the propagation of the laser and facilitate camera imaging.

The samples were obtained by moving the high-speed table on which the substrate is fixed and subsequently triggering the laser beam on the substrate. During fabrication, the high-speed camera records the creation and evolution of the molten pool. A delay is necessary to avoid acceleration effect on the sample.

2.2. Fabrication of the specimens

The material used in this study is a 316 L stainless steel, in the form of 3 mm thick, 30 mm wide and 75 mm long plates. The chemical composition of the plates is summarized in Table 1. Single fusion lines were achieved on these 316 L plates, using three set of process parameters, summarized in Table 2. Preliminary tests were achieved before the specimen fabrication to synchronize the different components of the bench (i.e. the laser beam with the table displacement, the lighting laser with the firing laser). In order to assess repeatability, three fusion lines of 30 mm length were performed for each set of parameters. In the following, fusion line samples will be designated according to the parameters set used (P1, P2 and P3).

2.3. Microstructural characterization

Microstructural analysis is carried out by optical microscopy (OM) and Electron Backscatter Diffraction (EBSD). In order to prepare the samples for metallurgical characterization, the plates containing fusion lines are cut and coated in a conductive resin, polished using SiC sand paper (1200, 2400), and finally polished with 6, 3, and 1 μm diamond suspensions. Once prepared, the samples are either prepared for OM or for EBSD. In the first case, the samples are etched with an aqua

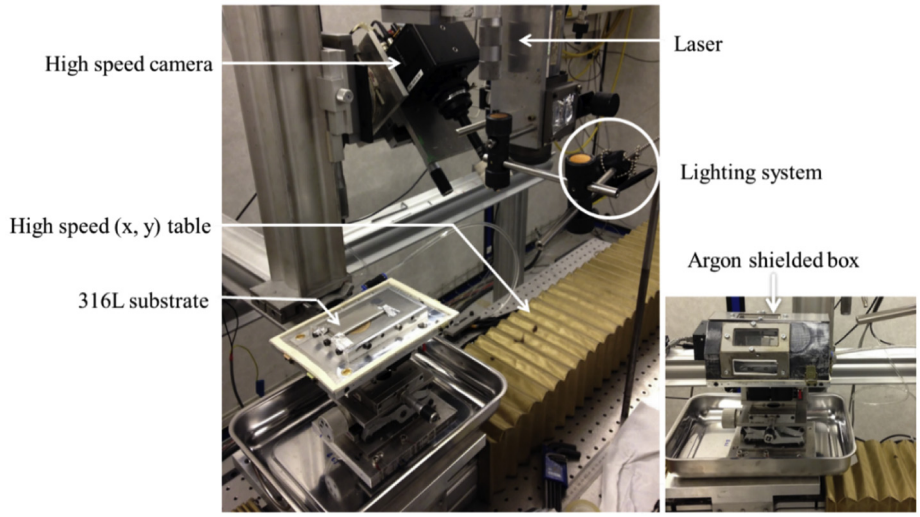

Fig. 1. Laser Powder Bed Fusion installation (PIMM-ENSAM, France).

Table 1
Chemical composition of the 316 L plates used in this study.

Elements	Cr	Ni	Mo	Mn	Si	N	O	C	Fe
Content (wt%)	17.3	12.0	2.36	1.89	0.33	0.047	0.0025	0.024	Balance

regia solution consisting of 10 mL of HNO_3 and 20 mL of HCl for 20 s, revealing the solidification limits and grain boundaries. For EBSD analysis, the samples undergo a final polishing step using a 0.06 μm colloidal silica suspension. EBSD is performed with a JEOL JSM-IT300 Scanning Electron Microscope (SEM) operating at 20 kV in backscattered electron mode (BSE). Data are processed using CHANNEL 5 (Oxford Instruments).

3. Modelling approach

In order to simulate grain structure formation during the LPBF process, two models are needed: a thermal one based on Finite Element (FE) method that models the thermal effects induced by the laser, and a metallurgical one based on Cellular Automaton (CA) that models solidification during LPBF. The coupling of the two is known as "CAFE" modelling. Both models are described in the following sections.

3.1. Thermal modelling

To model and analyse temperature variations during laser melting, a three-dimensional FE model is used. The simulations are carried out using the Cast3M software [35]. Note that only fusion lines are simulated in this study, for comparison to experimental results.

3.1.1. Mesh definition

In order to reduce computation time, only a part of the substrate ismeshed. Dimensions of the meshed substrate are 2.65 mm × 1.4 mm × 0.25 mm. The type and size of the elements vary within the mesh, depending on their location (Fig. 2). The elements located in the displacement axis of the laser (represented in red) are hexahedral and finely meshed while the others get larger and coarser as they stray from this axis (from the green to the blue zone).

Table 2
Laser power (P), travel speed (v) and corresponding linear energy chosen for the three set of process parameters.

	P (W)	v (mms^{-1})	P/v (Jmm^{-1})
P1	320	400	0.8
P2	400	400	1
P3	400	310	1.29

3.1.2. Thermal modelling

During laser melting, heat dissipates through convection, radiation and mainly by conduction in the substrate. Radiation and convection are taken into account with an equivalent heat exchange coefficient in a boundary condition model (see section 3.1.5). A thermo-conductive model is adopted, governed by the Fourier heat conduction equation:

$$\rho C_p \frac{\partial T}{\partial t} = div\left(\lambda.\overrightarrow{\nabla T}\right) + q \quad (1)$$

where T is temperature (K), q volumetric heat source contribution (W/m^3), ρ material density (kg/m^3), λ thermal conductivity (W/mK), C_p specific heat capacity (J/kgK) and $\overrightarrow{\nabla T}$ thermal gradient (K/m).

3.1.3. Heat source definition

To model the laser energy input, a volumetric heat source model defined by Goldak [36] is adopted, consisting in a double ellipsoid and characterized by:

- 4 geometrical parameters represented in Fig. 3: half-width (a), penetration (b), front and rear half-length of each ellipsoid, (c_f) and (c_r) respectively;

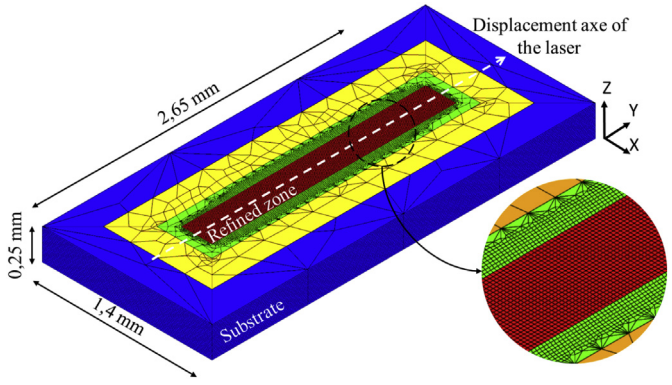

Fig. 2. Geometry and mesh of the samples.

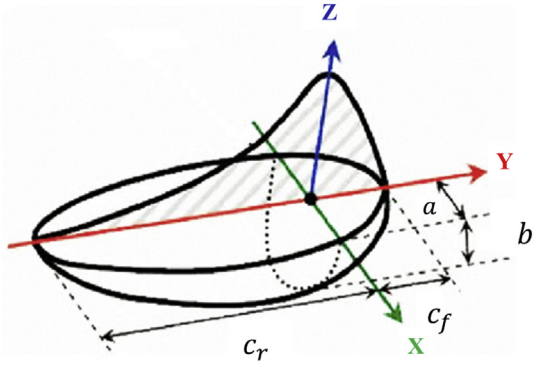

Fig. 3. Schematic representation of Goldak volumetric heat source.

- the total power Q (W) allocated in the volume, corresponding to the effective laser power *P*, i.e. the laser power corrected by the process efficiency, η. Q is a function of the geometrical parameters characterizing the volumetric power densities distribution at the front (q_f) and at the rear (q_r) of the heat source, according to the following equations:

$$Q = P\eta = \int_{-\infty}^{+\infty}\int_{-\infty}^{+\infty}\int_{-\infty}^{0}\left(q_f(x,y,z) + q_r(x,y,z)\right)dxdydz \tag{2}$$

$y<0$

$$q_r(x,y,z) = \frac{6\sqrt{3}Q\left(\frac{2}{1+\frac{c}{c_f}}\right)}{abc_r\pi\sqrt{\pi}}\, exp\left(-3\left(\frac{(x-x_0)^2}{a^2} + \frac{(y-vt-y_0)^2}{{c_r}^2} + \frac{(z-z_0)^2}{{b_u}2}\right)\right) \tag{3}$$

$y>0$

$$q_f(x,y,z) = \frac{6\sqrt{3}Q\left(\frac{2}{1+\frac{c}{c_f}}\right)}{abc_f\pi\sqrt{\pi}}\, exp\left(-3\left(\frac{(x-x_0)^2}{a^2} + \frac{(y-vt-y_0)^2}{{c_f}^2} + \frac{(z-z_0)^2}{{b_u}^2}\right)\right) \tag{4}$$

In order to determine the appropriate values of the heat source parameters, instrumented experiments are conducted (see section 2). These experiments allow for the observation of the shape and dimensions of the molten pool during the fusion lines. The geometric parameters of the heat source model are chosen as functions of the beam diameter. The focal spot size of the beam used in the instrumented bench being of 150 μm (2.1), the half-width a and the front and rear half-lengths c_f and c_r are fixed to 75 μm. The penetration is fixed to 50 μm. Then, numerical and experimental molten pool sizes are compared to determine the appropriate efficiency of the heat source (see section 4.2.1). The values of the heat source's function are given in Table 8.

3.1.4. Material properties

The heat capacity C_p (J/kgK), density ρ (kg/m^3) and thermal conductivity λ (W/mK) of the bulk material are temperature-dependant. The values used for the 316 L are those from Depradeux [37].

The latent heat of fusion is considered in the model by a virtual increase of the specific heat capacity in the solidification temperature interval.

3.1.5. Initial and boundary conditions

The initial temperature of the system T_0 is 293.15 K. In this study, radiation and convection are modelled by an equivalent heat flux φ_{eq} (W/m^2) applied on the edges of the part as shown below:

$$\varphi_{eq} = h_{eq}.(T_\infty - T) \tag{5}$$

where h_{eq} is an equivalent heat exchange coefficient (10 W/m^{2}K) and *T* and T_∞ the temperatures of the part surface and the outer respectively (K). T_∞ is fixed at 293.15 K during the calculation.

Only a small part of the substrate's thickness is modelled (see Fig. 2). To consider the influence of the heat conduction into the depth of the substrate on the heat transfer, an equivalent heat flux is imposed on the lower edge of the mesh, defined using eq. 5 with h_{eq} equal to 1000 W/m^{2}K. To determine this value, several simulations were performed, in which the first one considered a 3 mm thick substrate. The resulting thermal fields were compared to those obtained for a thin 0.25 mm thick substrate with different values of h_{eq} imposed on the lower side. The thermal fields of the 0.25 mm thick substrate are quasi-identical to those of the 3 mm thick one when using the calibrated heat coefficient.

3.2. Solidification modelling

The grain growth model is based on the cellular automaton (CA) model defined by Gandin and Rappaz [25]. It focuses on grain structure evolution during solidification. The solidification phenomenon in LPBF is controlled by two physical mechanisms: at the melt pool border, the epitaxial growth of the partially melted grains of the substrate, and in the undercooled liquid, the nucleation of new grains. No nucleation model is described in this study due to the fact that this last phenomenon was not observed during LPBF of 316 L material. In this section the CA method is briefly presented, then the grain growth's model is detailed.

3.2.1. Cellular automaton

The CA method [38] is characterized by the following. First, the material is discretized in regular cubic elements called cells, denoted by an index ν. Secondly, several variables are associated to each cell, the main ones being the state (I_ν), the temperature (T_ν) and the crystallographic orientation of the grain to which the cell belongs (see section 3.2.3).

In this work, four different states are defined:

- $I_\nu = 0$: **liquid** cell, if it is located in the liquid zone;
- $I_\nu = 1$: **mushy** cell, when the cell is located at the solid-liquid interface. This cell is able to grow, i.e. to be part of a growing grain;
- $I_\nu = 2$: **solid** cell, which means that the cell can't grow any further;
- $I_\nu = 3$: **ghost** cell, corresponding to an existing cell not taken into account during the CA calculation.

Once the cell network is characterized, the neighbourhood need to be described. Different orders of neighbouring exist. In this study, the neighbouring cells until the third order are considered, which includes the cells sharing a face, an edge and a corner with the central cell. In total, the neighbourhood is composed of 26 cells (Fig. 4).

Finally, transition rules are defined. They are responsible for the state and variables evolution of the cell. They are mainly based on the cell temperature and on the characteristics of the neighbouring cells, and enable us to model grain growth.

3.2.2. Transition rules definition

At the beginning all the cells are in the solid state ($I_\nu = 2$). During the LPBF process, some cells are subjected to the laser melting, resulting in a state transition from solid to liquid or mushy, and then cool down, transitioning from liquid to mushy state and finally from mushy to solid state. The transition rules depend on the initial state of the cell, its temperature and on the state of its neighbouring cells. An existing non-liquid cell ($I_\nu = 1$ or 2) becomes liquid when its temperature exceeds the liquidus temperature T_{Liq}. As a cell reaches the liquid state, its crystallographic properties are deleted and the solid cells located in its neighbourhood become mushy. Conversely, a liquid cell ν turns into a mushy cell if at least one of the mushy neighbouring cell μ

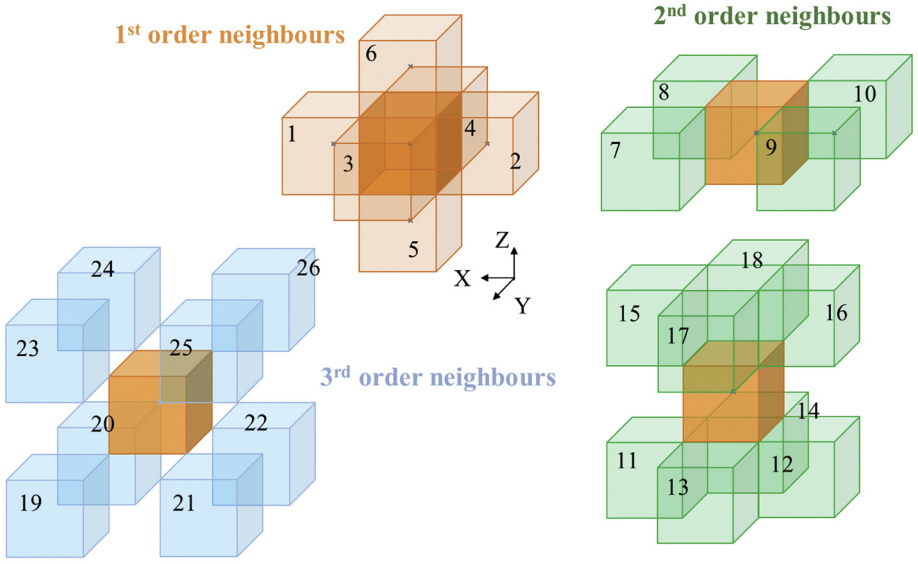

Fig. 4. Schematic representation of the neighbourhood of the ν cell, represented in orange.

grows up to its centre C_ν, and if its temperature T_ν is lower than $T_{Liq.}$ Finally, a mushy cell becomes solid when there is no more liquid cell in its neighbourhood. All these transition rules are resumed in Table 3.

3.2.3. Initial grains structure modelling

The initial grain structure of the substrate shows an almost equiaxed morphology. To accuratly model this structure, a Voronoi partition is preliminary made [39].This partition is necessary when initializing the cells in the CA model, since it enables the growth of the cell structure from the initial grain structure of the substrate. Consequently, all the CA cells gathered in a same Voronoï element will have the same grain characteristics, representing one grain. The mean diameter of the Voronoi elements has been chosen according to the grain size experimentally measured in the substrate. A cristallographic orientation characterized by the three Euler angles $(\varphi_1, \varnothing, \varphi_2)_\nu$ is attributed to each Voronoi element, calculated as follows:

$$\begin{cases} \varphi_1 = 2\pi\,(0,5-u_1)+\pi & \varphi_1 \in [0,2\pi] \\ \varnothing = \arccos\,(1-2u_2) & \text{with} \quad \varnothing \in [0,\pi] \\ \varphi_2 = 2\pi\,(0,5-u_3)+\pi & \varphi_2 \in [0,2\pi] \end{cases} \tag{6}$$

where u_1, u_2 and u_3 are randomly chosen between 0 and 1.

Once the initial grain structure has been defined using the Voronoï partition, each CA cell is associated to a grain number, and the Euler angles of this grain are affected to the cell.

3.2.4. Grain growth modelling

The model of grain formation is based on the work of Gandin et al. [40]. After solidification, austenitic stainless steels form a face centred cubic (FCC) network. In the present model, only the mushy cells are able to grow. The grain growth begins at the molten pool edge, where some cells modelling the substrate are in contact with the liquid zone, turning into mushy cells. To precisely model grain formation and to avoid the influence of cell geometry on grain growth, an envelope is attributed to the growing cells. As visible in Fig. 5, this envelope is a regular octahedron centred on the cell ($C_\nu = C_\nu^{en}$, C_ν being the centre of ν cell and C_ν^{en} the centre of its envelope) with its six apexes representing the ⟨100⟩ crystallographic directions (preferential growth directions for cubic metals) and so the primary dendritic arms of the grain. The grain is characterized by a unique index and a crystallographic orientation, depending on Euler angles, $(\varphi_1, \varnothing, \varphi_2)$. Just after the transition from solid state to mushy state, for the cells in the substrate directly in contact with liquid cells, the initial envelope of the cell is created. It is centred on the cell and the initial length of its arms ($R_\nu^{t_0}$) is zero (see (a) in Fig. 6).

The apexes of the octahedron correspond to the primary dendrites' arms. Consequently, its ends represent the dendrites tips of the crystal. The grain growth model is therefore based on dendrite tip growth. This part of the model is divided into three steps: the dendrite growth kinetics, the capture and the envelope formation, described in the following.

Table 3
Transition rules for the melting and growth of a v cell neighbour of a m cell.

Transition	Initial state	Transition rules	Final state
Melting	$I_\nu = 1$ or 2	$T_\nu > T_{Liq}$	$I_\nu = 0$
	$I_\nu = 2$	$\exists I_\mu = 0$	$I_\nu = 1$
Growth	$I_\mu = 0$	$T_\mu^{t+\delta t} < T_{Liq}$ $\exists\, I_\nu = 1$ with $\lvert x_\mu^\nu\rvert + \lvert y_\mu^\nu\rvert + \lvert z_\mu^\nu\rvert \le R_\nu^{t+\delta t}$ (see section 3.2.4)	$I_\mu = 1$
	$I_\nu = 1$	$\exists I_\mu = 0$	$I_\nu = 2$

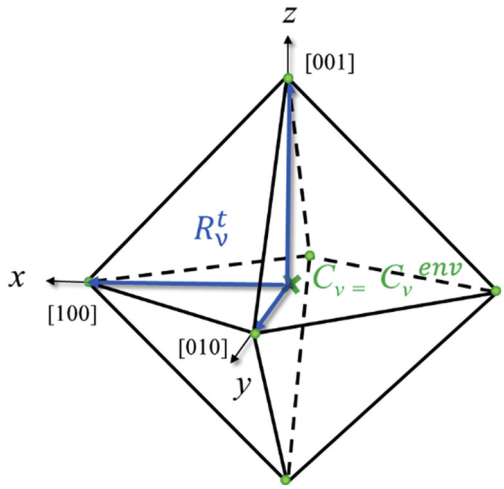

Fig. 5. Regular octahedral envelope of the grain nuclei on the v cell.

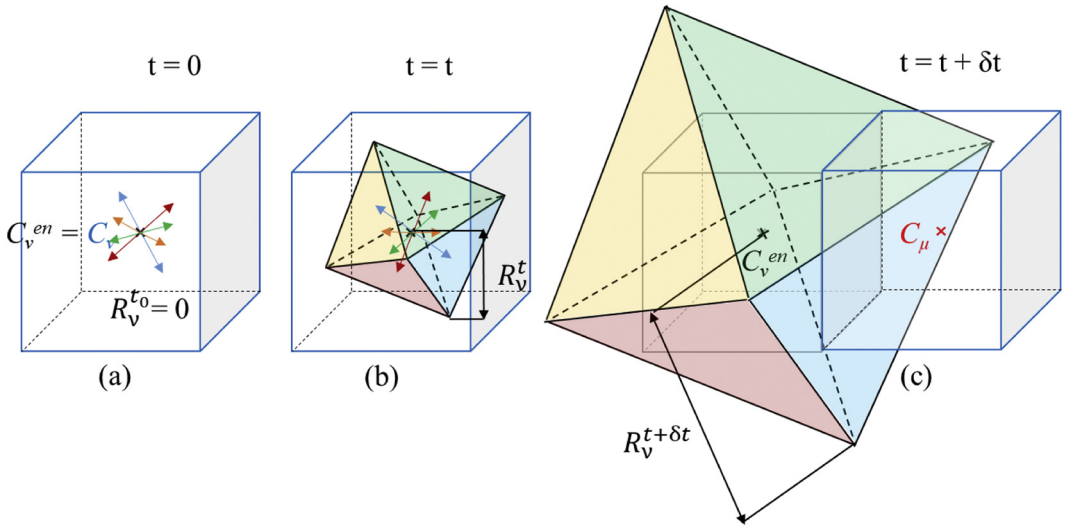

Fig. 6. (a) Creation and (b) growth of the envelope of the ν cell; (c) capture of the μ cell by the envelope of the ν cell.

• Dendrite growth kinetics

The growth velocity v of the dendrite tips is calculated as follows:

$$v(\Delta T_\nu) = a\Delta T_\nu{}^n \tag{7}$$

or

$$v(\Delta T_\nu) = a_1\Delta T_\nu + a_2\Delta T_\nu{}^2 + a_3\Delta T_\nu{}^3 \tag{8}$$

where ΔT_ν is the undercooling at the dendrite tip in K.

Three growth kinetic laws are compared in our modelling, corresponding to various sets of parameters a and n or a_i. The two first ones are those retained by Zinovieva et al. for a 316 L stainless steel [21] and by Tan and Shin for a 304 [42]. In the third model, the parameters a and n are numerically determined from the theoretical model proposed by Kurz et al. [34], using the physical properties of the 316 L and the temperature gradients computed from the thermal simulations of the fusion lines given in Table 4. The model parameters are resumed in Table 5.

Once ν is determined, the envelope extension $\Delta R_\nu^{t+\delta t}$ is given by

$$\Delta R_\nu^{t+\delta t} = v(\Delta T_\nu)\delta t \tag{9}$$

where δt is the micro time-step. The resulting length of the apex is simply calculated by adding the extension to the apex length at the beginning of the time step R_ν^t (see (b-c) in Fig. 6):

$$R_\nu^{t+\delta t} = R_\nu^t + \Delta R_\nu^{t+\delta t} \tag{10}$$

• Capture

During the envelope's growth, the octahedron may encompass the centre of a neighbouring liquid cell, μ. This is known as the "capture".

Table 4
Physical properties and process characteristics retained for the calculation of our grain growth model.

Parameter	Value	Reference
Liquid inter-diffusion coefficient D_l (m^2s^{-1})	3×10^{-9}	[41]
Gibbs-Thomson parameter Γ (mK)	2×10^{-7}	[41]
Initial liquid composition C_0 (%)	31%	[41]
Liquidus slope ml (K/wt%)	−2.5	[41]
Partition coefficient k	0.65	[41]
Temperature gradient Gl (K/m)	1×10^6–2×10^7	This study
Growth speed V (m/s)	0.08–0.4	This study

This stage is crucial in modelling grain growth because it enables the transmission of the crystallographic information of a cell to its neighbours, allowing the formation of the grain. Indeed, all the cells with the same crystallographic orientation and state index constitute a grain.

To be captured at eatch δt time-step, a given cell μ should fulfil two conditions: be under the liquidus temperature at the end of the time-step ($T_\mu^{t+\delta t} < T_{Liq}$) and have at least one neighbour ν able to grow ($I_\nu^{t+\delta t} = 1$). If these two conditions are fulfilled, the position of the centre of μ (C_μ) is studied regarding the position of the envelope of ν (Fig. 6. (c)). To this end, the coordinates of the centre of μ cell is expressed in the octahedral local system associated to the envelope of ν using the transition matrix defined by Bunge [43], calculated as follows:

$$g_\nu = \begin{pmatrix} cos\varphi_1.\cos\varphi_2 - sin\varphi_1.\sin\varphi_2.cos\phi & sin\varphi_1.\cos\varphi_2 + cos\varphi_1.\sin\varphi_2.cos\phi & sin\varphi_2.sin\phi \\ -cos\varphi_1.\sin\varphi_2 - sin\varphi_1.\cos\varphi_2.cos\phi & -sin\varphi_1.\sin\varphi_2 + cos\varphi_1.\cos\varphi_2.cos\phi & cos\varphi_2.sin\phi \\ sin\varphi_1.sin\phi & -cos\varphi_1.sin\phi & cos\phi \end{pmatrix} \tag{11}$$

Then the coordinates are compared to the apex length at the end of the time step $R_\nu^{t+\delta t}$. In the event that several neighbours capture the μ cell, it is considered that the capturing cell is the one that grew the most during the time-step.

• Envelope formation for a captured cell μ

After being captured, the previously liquid cell μ becomes a growing cell that has the same crystallographic information (same grain number and Euler Angles) as its capturing neighbour ν. Consequently:

$$I_\mu{}^{t+\delta t} = 1 \tag{12}$$

$$(\varphi_1, \varnothing, \varphi_2)_\mu = (\varphi_1, \varnothing, \varphi_2)_\nu \tag{13}$$

$$n_{grain}{}^\mu = n_{grain}{}^\nu \tag{14}$$

To be able to grow and then to transmit the crystallographic information, the cell needs its own envelope. The creation of an envelope

Table 5
Parameters of the three studied growth models corresponding to eqs. (7) and (8).

Parameters	a	a_1	a_2	a_3	n
Zinovieva model [21]	–	0	2.49×10^{-7}	6.2×10^{-8}	–
Tan model [42]	7.325×10^{-6}	–	–	–	3.12
Our model	1×10^{-8}	–	–	–	4.8

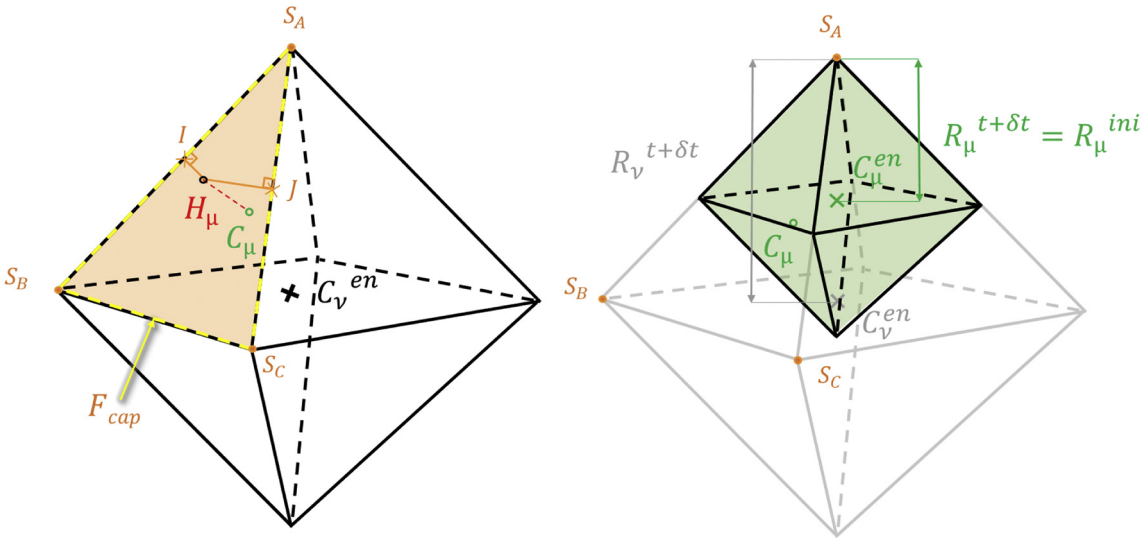

Fig. 7. Illustration of the envelope formation of the μ cell after being captured by the ν cell.

for a captured cell differs from the creation of an initial one. The main steps are presented here and are illustrated in Fig. 7:

1. Identify the capturing face (F_{cap}) of the octahedron;
2. Spot the apex (S_A) of the octahedron which is the closest to the centre C_μ;
3. Calculate the coordinates of H_μ, the point on F_{cap} where C_μ projects;
4. Based on the length IS_A and JS_A, I and J being the orthogonal projections of H_μ on $[S_AS_B]$ and $[S_AS_C]$ segments respectively, calculate the initial envelope size of μ, $R_\mu^{t+\delta t} = R_\mu^{ini}$;
5. Finally, place the centre of the new envelope of μ C_μ^{en}, and convert its coordinates in the global coordinate system.

3.3. CAFE model

As explained in the previous sections, two models are defined and coupled in the CAFE approach: a thermal FE model and a solidification CA model. In this study, a weak coupling is adopted: the temperatures computed using the FE model are transmitted to the solidification model, whereas the solidification grain evolution has no influence on the thermal model. The transmission of the temperatures is performed by:

- superimposing the FE mesh on the cell network. Here every cell is associated to a given finite element;
- interpolation of the temperatures onto the centre of the cell. The temperature at the centre of the cell is computed by interpolating the temperatures at the nodes of the corresponding element.

Two different time steps are defined in the CAFE model. The first one is fixed ($\Delta t = 20\ \mu s$) and is used for the thermal computation. The second one is used for the CA calculation and varies depending on the maximum growth velocity of the dendrites $\delta t = \min(\Delta t, l_{CA}/max(v(\Delta T))$, l_{CA} being the length of a cell and $v(\Delta T)$ the growth velocity). If no cell is able to grow, $\delta t = \Delta t$. Therefore, several CA computations can be done for each thermal FE iteration.

3.4. Validation of the grain growth algorithm

Validation of the CA model is necessary before testing it on a laser melting configuration. This step consists in reproducing several cases of the literature in order to validate the main stages of the solidification algorithm.

The first studied case consists in the growth of a 3D monocrystal positioned in the centre of a cubic cells network subjected to a uniform thermal gradient ($G = 250\ K/m$, towards Z axis), and with a constant cooling rate ($\dot{T} = -0.1\ K/s$). More details on this configuration are presented in the work of Gandin et al. [44]. Fig. 8 shows the resulting grain

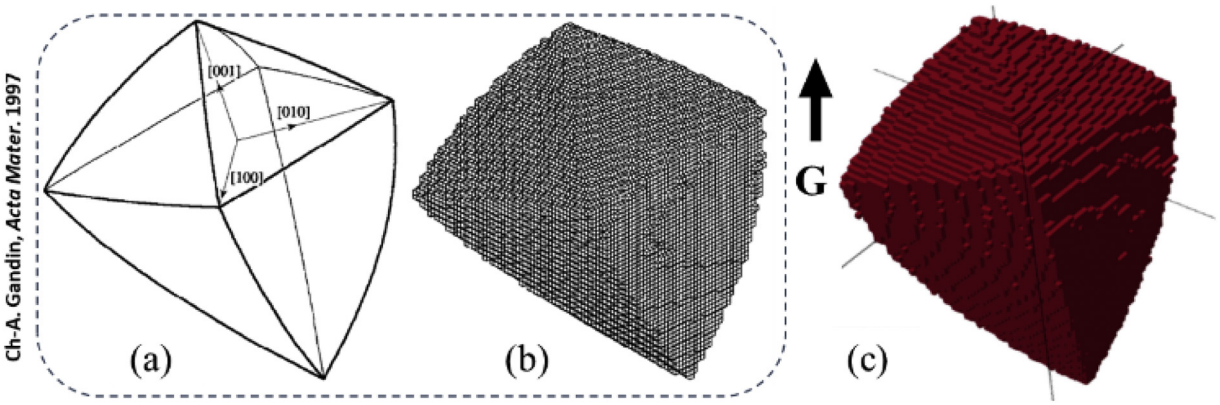

Fig. 8. Results of monocrystal growth obtained by Gandin et al. [44] (a) analytically and (b) numerically, and (c) obtained numerically using the model presented in this study.

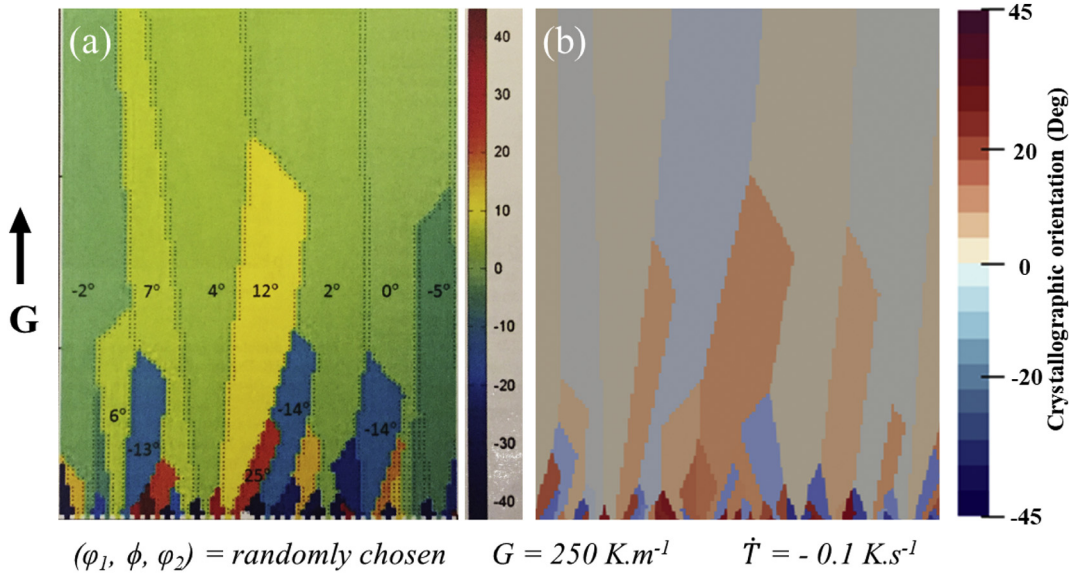

Fig. 9. Numerical results of the competition growth of crystals obtained by (a) Rai et al. [22], and (b) using the model presented in this study.

morphology obtained after cooling. Grain growth is faster in the opposite direction of the thermal gradient (−Z), due to the fact that the undercooling is higher in this area. The 3-dimensional grain obtained with the algorithm presented in this study (Fig. 8. (c)) is similar to the one obtained by Gandin et al. [44], so the grain growth step of the algorithm is considered valid.

The second test is two-dimensional and was published by Rai et al. [22]. The same thermal gradient and cooling rate as Gandin's case are used ($\dot{T} = -0.1\ K/s$ and $G = 250\ K/m$ towards Z axis) but with a rectangular geometry where small germs with different crystallographic orientations are fixed to the bottom side. As seen in Fig. 9 columnar growth of the grains having the smallest disorientation in relation to the thermal gradient (angle close to 0) is favoured, and this growth prevents the growth progression of the grains with the largest misorientation. As a result, the number of grains decreases as solidification progresses. Therefore, this result indicates that the algorithm correctly models grain growth competition.

4. Results and discussions

4.1. Experimental results

The fusion line samples produced were analysed focusing on two kinds of data. First, the shape and size of the melt-pools were observed and measured, in order to compare the various samples and to calibrate and validate the FE thermal model. Secondly, the grain size and morphology in the substrate and molten zone were analysed, for comparison with the results obtained with the CA simulations. Cross sections of fusion line samples are shown in Fig. 10. One can see that the width and depth of the melt-pool increase with the linear energy P/v.

Fig. 11 shows images in a top view of the molten pools recorded during the process using a high-speed camera fixed at the laser's reference frame. Only the stationary zones of the samples are presented in this study. The global shape is similar for the three kinds of samples, but the molten pool elongates when the linear energy increases. The average dimensions of the samples are summarized in Table 6. The values of every sample are calculated from three cross-sections and forty top views. One can observe the elongation ratio L/W and the penetration ratio D/W both increase with the linear energy. However, the elongation ratio is more influenced by a power change than by a travel speed change.

Fig. 14 shows the Z direction Inverse Pole Figure (IPF) colour map obtained from EBSD analyses in a cross section of fusion line P2. One can observe a change in the grain morphology between the substrate having an equiaxed grain structure, and the molten zone showing a columnar grain structure. This kind of structure is consistent with the results usually observed experimentally in the literature for a 316 L obtained by LPBF [6,10,13,14].

The averages cross-sectional area of the grains and the associated equivalent diameters and aspect ratios calculated from this EBSD map are summarized in Table 7. The average size of the grains located in the molten zone is lower than the mean size of the grains constituting

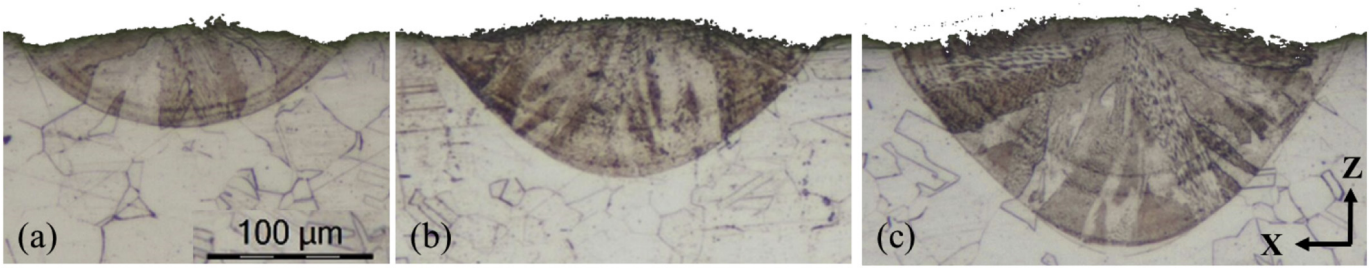

Fig. 10. Cross sections of fusion lines obtained with various power and travel speed: (a) P1, 320 W – 400 mms^{-1}, (b) P2, 400 W - 400 mms^{-1}, (c) P3, 400 W – 310 mms^{-1}.

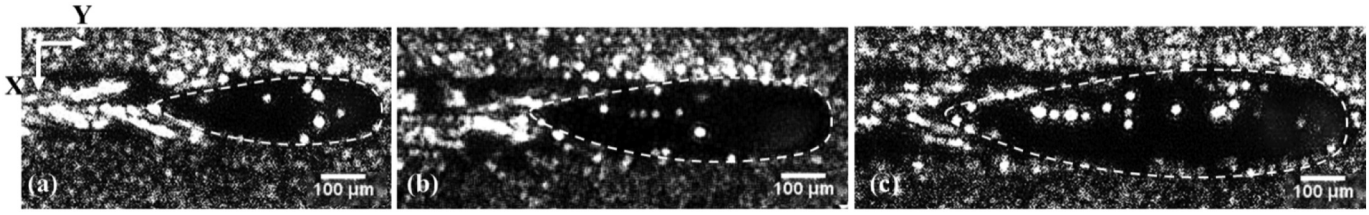

Fig. 11. Top views of the melt-pools extracted from high speed camera recording (a) 320 W - 400 mms^{-1} (b) 400 W - 400 mms^{-1} (c) 400 W - 310 mms^{-1}.

Table 6
Dimensions of the molten pool experimentally measured on the three kind of samples.

Sample	Width W (µm)	Depth D (µm)	Length L (µm)	*L/W*	D/W
P1	211	60	500	2.37	0.28
P2	225	88	710	3.15	0.39
P3	269	125	872	3.24	0.46

Table 7
Grain characteristics measured from EBSD analyses on cross section of sample P2.

	Average cross-sectional area (µm^2)	Average diameter (µm)	Average aspect ratio
Melting zone	380	22.0	3.4
Substrate	509	25.5	1.5

the substrate. In addition, one can see that the aspect ratio in the molten zone is more than twice as high as the substrate's one, which is consistent with the columnar shape of the grains observed.

The IPF Z colours map also indicates that in the centre of the melting zone, the grains coloured in red and pink (i.e. having <100> crystallographic direction almost parallel to the Z axis) are longer than the green or blue ones. This is consistent with the fact that in Face Cubic Centred (FCC) structures, the preferential growth directions are the <100> directions. Consequently, the grains having this orientation parallel to the thermal gradient (i.e. parallel to the Z axis in the centre of the melting zone) grow farther than the other ones, partly stopping the growth of less favourably oriented grains.

Contrarily, at the edge of the melting zone, the thermal gradient is at an angle to the vertical axis, promoting the growth of grains having a <100> crystallographic direction rather parallel to this inclined direction. Thus, the fast-growing grains are those with a ⟨111⟩ or ⟨110⟩ direction parallel to the Z axis, what could explain why the green and blue colours are predominant on the edges of the melting zone.

One can also notice that there is no marked grain texture in the molten zone, unlike what was observed in other studies relating to multilayer LPBF samples [32]. The lack of texture can be explained by the various directions of the thermal gradient during the deposit of a fusion line, which is normal to the solid/liquid interface, and then promotes various crystallographic growth directions depending on whether the grains are in the centre or on the edges of the melt pool.

Table 8
Retained parameters of the heat source model.

Parameters (µm)	a	b	c_f	c_r	Q		η
						P1	0.33
	75	50	75	75	400.η	P2	0.4
						P3	0.43

4.2. Thermal modelling results

4.2.1. Heat source calibration

As presented in section 3.1, the parameters of the heat source model have to be calibrated to correctly model the melt-pool dimensions. In order to simplify the calibration process, the values of the geometrical parameters were chosen from the diameter of the laser beam, and only the efficiency of the laser was adjusted to fit the width and length of the experimental melt-pool for each fusion line shown in section 4.1. Note that for this calibration, the border of the numerical melt-pool is supposed to be delimited by the liquidus isothermal surface.

The retained parameters of the heat source model for the simulations of the three fusion lines are summarized in Table 8, and the dimensions of the molten pool (numerical and experimental) in Table 9. A good agreement between the experimental and numerical width and length is observed (error < 5% except for the width of P1 which is of 9%), but on the contrary, the numerical depth is higher than the experimental one (7 to 32% of error). Our objective was to develop a rapid and robust calibration method based on simple observations of the manufactured samples, as the melt-pool surface. Consequently, the thermal simulation results were considered to be sufficiently in agreement with the experiment to simulate the grain formation. The gap between experimental and numerical depth could be reduced by calibrating also the four geometrical parameters, in addition to the efficiency. But this is a rather long and complicated operation, that require in addition to prepare a cross-section of each new sample, which is not always applicable for a manufactured component.

4.2.2. Thermal results

The results of thermal simulation allow for the estimation of the growth rate or solidification rate R (m/s), and the thermal gradient G (K/m) along the solidification front, both parameters controlling the grain structure morphology and size. G directly results from the simulations and R is calculated by multiplying the product of the angle between the normal to the interface and the scanning direction by the scanning speed. The product of them, GR, expressed in K/s, controls the characteristic size of the microstructure and corresponds to the cooling rate of the material: the higher the cooling rate, the finest the microstructure will be [33].

Considering that the growth direction is normal to the liquidus surface, the growth rate R increases from the edge of the melt-pool to the

Table 9
Experimental and numerical melt-pool dimensions.

	Values (µm)	Experimental	Numerical	Error
P1	Width	211	193	−9%
	Depth	60	88	32%
	Length	500	500	0%
	Width	225	232	3%
P2	Depth	88	110	25%
	Length	710	741	4%
	Width	269	274	2%
P3	Depth	125	134	7%
	Length	872	839	−4%

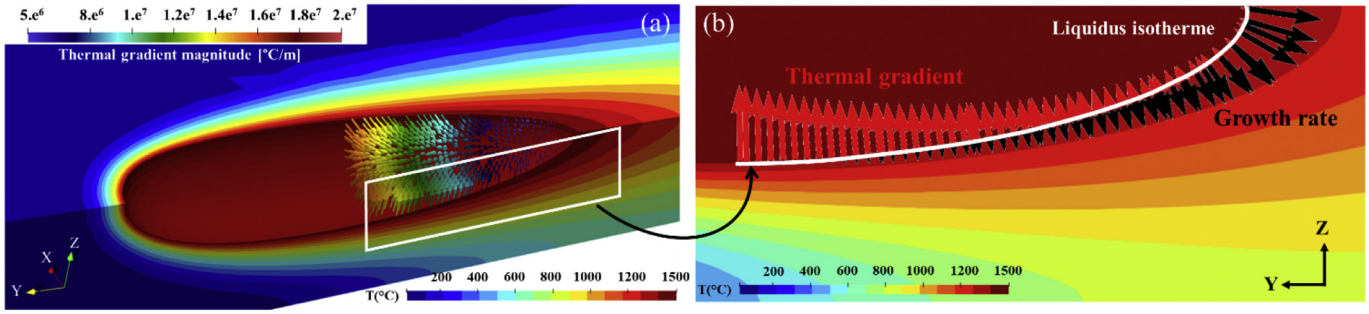

Fig. 12. Evolution of (a) the thermal gradient G and (b) the growth rate R along the solidification front for P2 simulation.

Table 10
Growth rate R, thermal gradient G, G/v ratio and cooling rate GR ranges deduced from thermal simulation for the three LPBF conditions.

	Growth rate range R (m/s)	Thermal gradient range G (K/m)	G/R range (Ks/m^2)	G.R range (K/s)
P1	0–0.4	2×10^7–5×10^6	∞–12.5×10^6	0–2×10^6
P2	0–0.4	1.17×10^7–3×10^6	∞–7.5×10^6	0–1.2×10^6
P3	0–0.31	1.5×10^7–1×10^6	∞–3.225×10^6	0–3.1×10^5

Table 11
Comparison of grains characteristics in cross-sections on the sample P2 calculated from experimental and numerical results.

		Average cross-sectional area (μm^2)	Average diameter (μm)	Aspect ratio
Substrate	Experimental	509	25.5	1.5
	Numerical	390	22.3	1.8
Fusion line	Experimental	380	22.0	3.4
	Numerical	546	26.4	3.0

centre, up to a value equal to the laser speed. On the opposite, the thermal gradient G decreases from the edge to the centre of the melt-pool, decreasing from about 1×10^7 K/m to about 3×10^6 K/m for the fusion line P2 (Fig. 12). Note that these values are very high and correspond to a rapid solidification condition defined by Kurz et al. for their model [34,45]. The ranges of growth rate and thermal gradient computed for each condition are resumed in Table 10. One can notice that the minimum value of the G/R ratio obtained in the centre line of the melt-pool decreases with the increase of the linear energy. This ratio controls the morphology of the solidification front, a decrease of this parameter promoting the evolution of the solidification front from cellular to columnar dendritic and finally equiaxed. In the same way, an increase of the linear energy produces a decrease of the maximal cooling rate given by GR, promoting coarser microstructures. However, the order of magnitude of G and R are similar for the three conditions, which means that the solidification conditions won't be fundamentally different.

4.3. CA simulation results

The results of the CAFE modelling of the fusion line P2 using our growth model are visible in Fig. 13, and on the videos linked to the web version. The CA domain is 2.5 mm long, 0.25 mm large and 0.12 mm deep, and composed of cells of 1 μm side. A mean diameter of 25 μm is chosen for the Voronoi partition in order to model the substrate structure. This value is sourced from the average equivalent sphere diameter of the grains measured in the 316 L substrate (see Table 11). It is important to specify that the colours visible in this figure correspond to the φ_1 value. Moreover, the dark blue zone visible in Fig. 13 corresponds to the molten pool. It can be noticed that grains form epitaxially from the grains of the substrate at the liquid-solid interface, and that they grow with a growth direction sensibly perpendicular to this surface. This observation is consistent with the work of Mutke et al. [46] and with our experimental results shown in Fig. 14 (a). Looking at the longitudinal section, it can be observed that the grains are elongated, slightly tilted towards the scanning direction and mainly oriented towards the *Z*-axis.

Numerical and experimental grain structures in cross-sections of sample P2 are compared in Fig. 14 and Table 11. Both experimental and numerical images show visible columnar grains, with perpendicular orientation with respect to the solid interface. Regarding the crystallographic orientation of the grain, both experimental and numerical EBSD scans reveal the lack of texture in the samples.

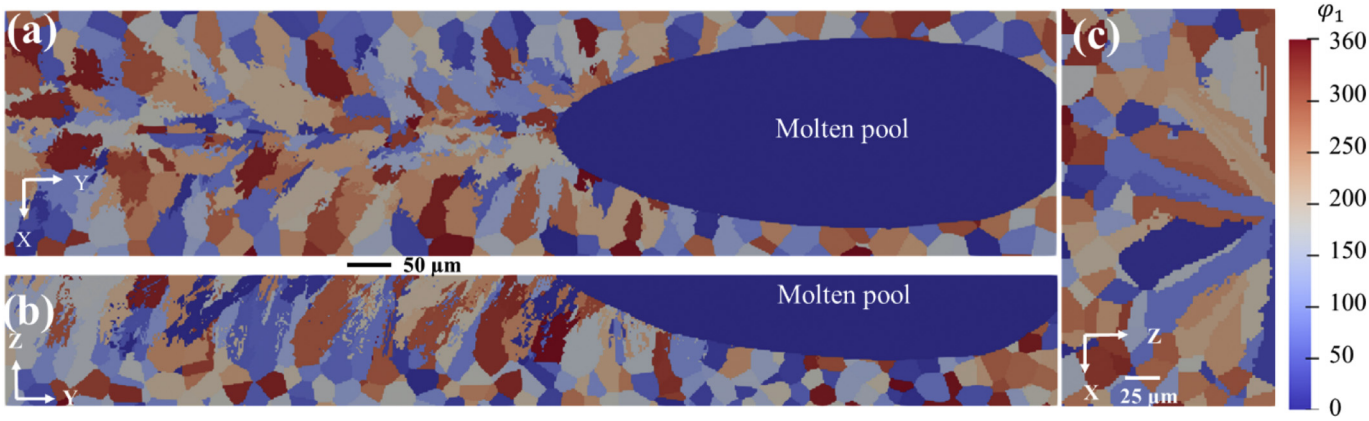

Fig. 13. Grain structure of the fusion line P2 obtained by numerical calculation using the CAFE model. (a) Top view, (b) longitudinal section and (c) cross section.

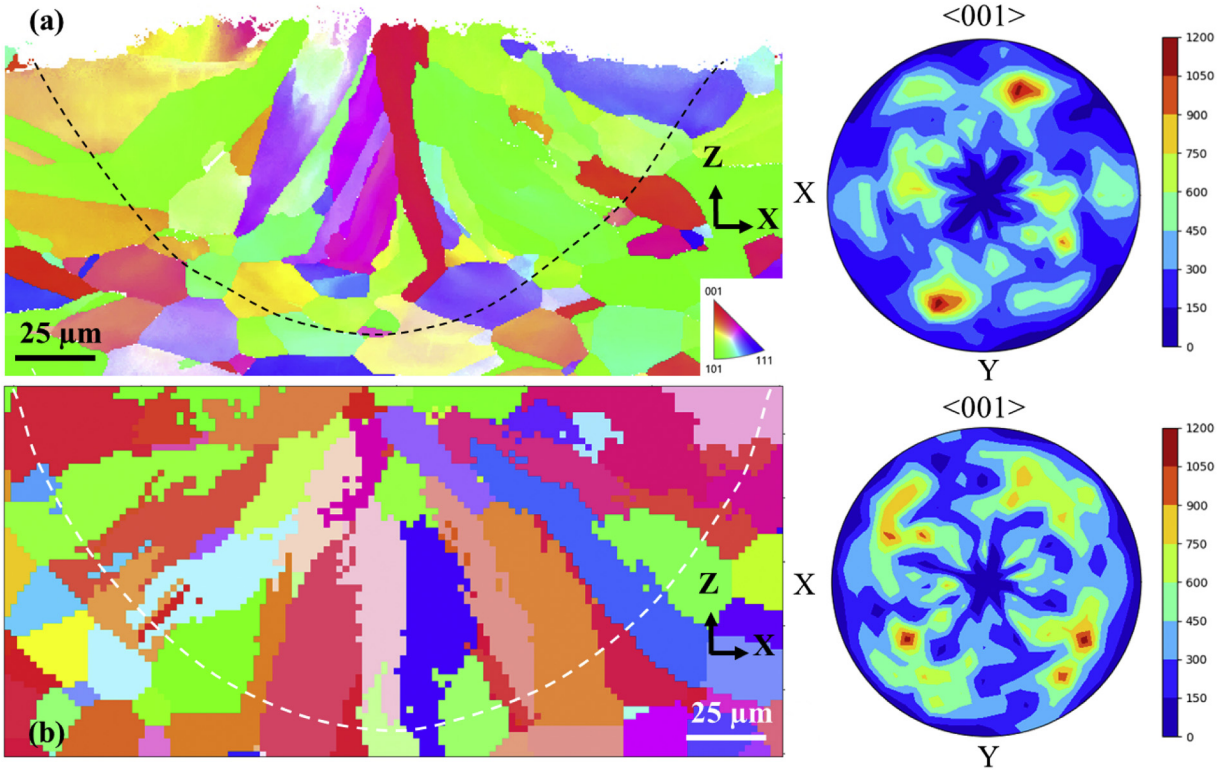

Fig. 14. Cross-sections of grain structure obtained for (a) experimental and (b) numerical fusion line P2. The associated pole figure represent the ⟨001⟩ directions in the normal to Z plane.

Looking at Table 11, both experimental and numerical aspect ratios reveal almost equiaxed in shape grains in the substrate. Regarding the size of the grains, it can be observed that numerical grains are smaller than the experimental ones in the substrate. The numerical substrate being composed of grains of noticeably identical size due to the Voronoï partition can justify this difference. The size of the numerical grains could be increase by changing the initial equivalent diameter for the Voronoï partition. However, apart from large grains, the averages cross-section area distribution is very close between experimental and numerical. Moreover, the aspect ratio of the numerical grains being only 20% higher than the experimental one, correlation between experimental and numerical grains size and morphologies in the substrate is thus rather good.

On the other hand, the average diameter of the numerical grains in the cross section of the molten zone is about 20% higher than the experimental one, and the aspect ratio is slightly lower in the simulation. A reason for these differences is the larger size of the numerical molten pool in the cross-sections, which is 18% deeper than the experimental one, promoting the formation of coarser columnar grains. The molten pool border on the experimental cross sections is also difficult to locate precisely, and it is possible that the assumed experimental molten pool includes some smaller grains of the substrate, decreasing the average grain size. Finally, it has to be noticed that the average grain size in the experimental molten pool is computed from EBSD analysis using only 78 grains, and only two of them have a cross-sectional area higher than 1000 µm^2 (Fig. 14 (a)). On the other hand, the numerical grain size is computed using more than 2400 grains, so a statistical effect is possible if the cross-section of Fig. 14 (a) is not representative of the global grain structure. Regardless, these numerical results are very promising and can be used to study the effect of LPBF process parameters on the solidification grain structure.

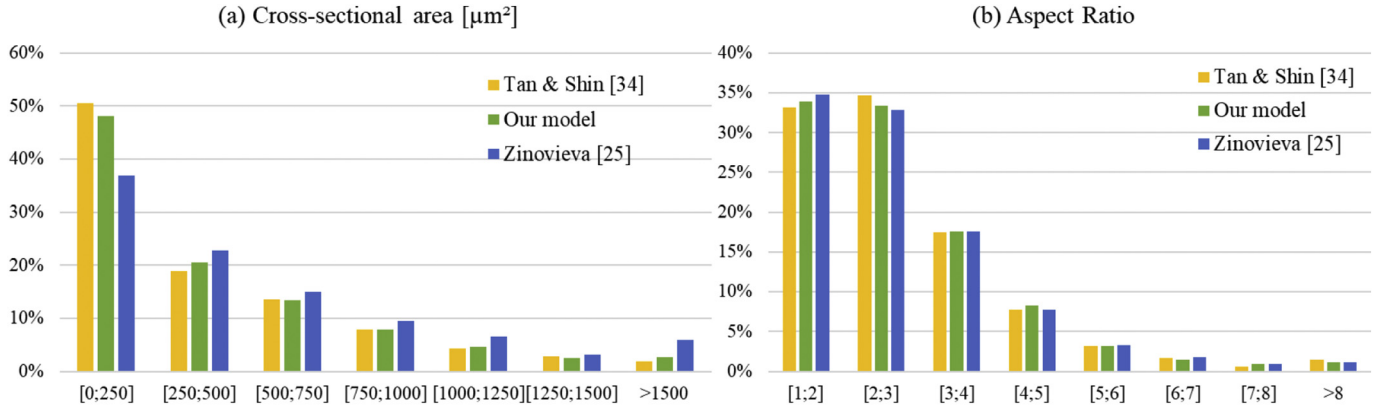

Fig. 15. Repartition of (a) cross-sectional area and (b) aspect ratio of the grains obtained with the three compared models for P2.

Table 12
Comparison of grains characteristics in cross-sections on the sample P2 calculated from numerical results obtained with different growth models.

Growth model	Average cross-sectional area (μm²)	Average diameter (μm)	Aspect ratio
Shin & Tan	518	25.7	2.99
Notre modèle	546	26.4	2.97
Zinovieva	641	28.6	2.74

Table 13
Comparison of grain characteristics in cross-sections on the samples P1, P2 and P3 calculated from numerical results.

	Average cross-sectional area (μm²)	Average diameter (μm)	Aspect ratio
P1	477	24.6	2.77
P2	546	26.4	2.97
P3	567	26.9	3.07

The grain structure characteristics obtained with the three growth models given in Table 5 are also compared. Fig. 15 and Table 12 show that Tan's model predicts a rather similar grain size and aspect ratio distributions than our model. On the other hand, the Zinovieva model predicts a higher percentage of largest grains (larger than 1500 μm²) than the two other ones. That could be explained by the minimal variation of the growth rate with respect to the undercooling in this model. When a grain is unfavourably oriented with respect to the thermal gradient direction, its growth is delayed and the undercooling at its dendrite tip increases. Inversely, the growth rate being directly related to the undercooling (defined by a power law), can consequently accelerate the grain's growth rate if the undercooling is increased. With the Zinovieva model, this increase does not seem sufficient to follow the growth rate of its neighbours more favourably oriented. Hence, these neighbouring grains become larger and occupy the undercooled liquid available due to the delay of the unfavourably oriented grains. As our model predicts larger grains compared to the experimental grains (Table 11), one can conclude that Zinovieva's model, which predicts still larger grains, is not suited for our process' conditions. Tan's model predicts similar grain sizes to our model, with a slightly lower average aspect ratio (Table 12), and thus, does not allow either an improvement of the growth model for the tested conditions.

Finally, the numerical grains characteristics of the three fusion lines conditions obtained using our growth model are compared. Fig. 16 shows the grains size and aspect ratio distributions in cross-sections obtained for the three conditions, and Table 13 presents the average characteristics calculated for each set of parameters. Note that the histograms were obtained from a grain population of more than 2000 for each condition, and can be considered as representative of the cross-sectional grain characteristics.

The first trend that can be deduced from these results is that for a constant power, a decrease of the travel speed produces a slight increase of the average cross-sectional area (4%), mainly due to the rise of the number of large grains (those having a cross-sectional area superior to 1000 μm²). In the same time, the aspect ratio of the grains increases a little for a constant power. On the contrary, one can observe that a decrease of the laser power at a constant speed leads to the reduction of the aspect ratio. It also generates more equiaxed in shape grains, and a decrease of the size of the grain by 12%, which is linked to the reduction of the number of largest grains.

These results indicate that when the linear energy (i.e. power/velocity ratio) increases, the average cross-sectional area of the grain and its aspect ratio increases too. An explanation to this observation comes from the slower cooling rate and the less pronounced thermal gradient generated at higher linear energy. The reduction of the thermal gradient and cooling rate leads to less marked temperature variations in the molten zone. Consequently, grains being late in comparison to their neighbours will not reach a high enough undercooling to catch up their gap. The increase of the linear energy thus favours grain growth competition between grains. These results indicate some tendencies that will allow in the future to optimize the grains characteristics (more or less equiaxed, more or less refined…) in view to improve the mechanical properties of the LPBF manufactured components.

5. Conclusions

A CAFE model was proposed to investigate grain formation during LPBF process of a 316 L stainless steel. It consists in a coupling of two models: a Finite Element model that studies thermal variations during the LPBF process, and a Cellular Automaton model for grain growth. The coupling is based on the transmission of the thermal fields resulting from the FE simulations to the CA model. Additionally, instrumented experimentation was conducted in order to help defining and validating the thermal model and to compare experimental grain characteristics with numerical ones. The main results of this paper can be summarized in the following points:

- Thermal model has been implemented and calibrated with regards to instrumented experimentations and first results are consistent in comparison with experimental results.
- CA model has been implemented and validated on test cases identified from the literature.

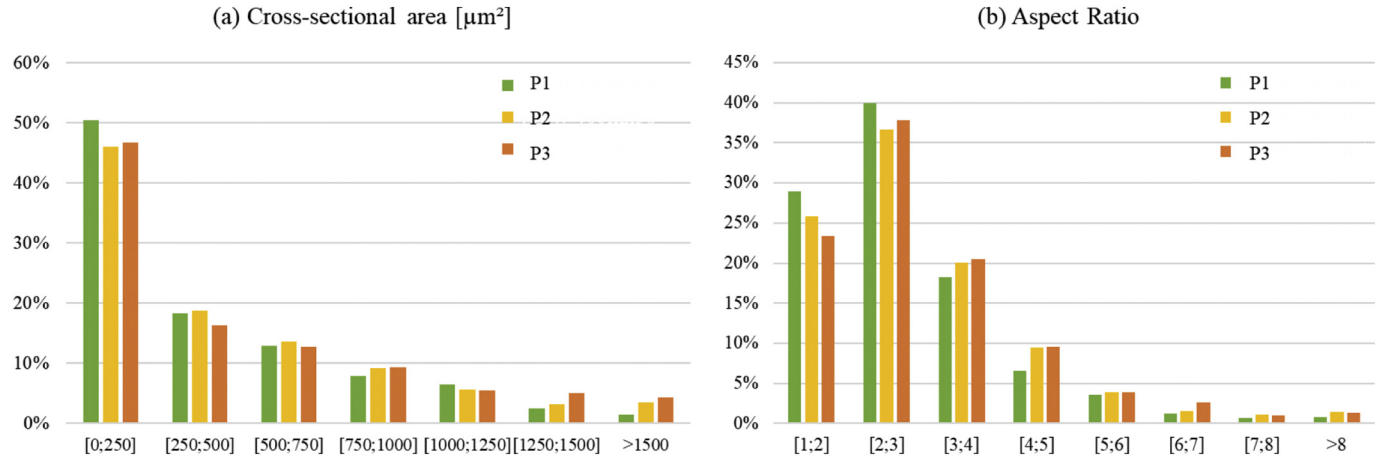

Fig. 16. Repartition of (a) cross-sectional area and (b) aspect ratio of the grains obtained with our growth model for the three LPBF conditions.

- A first coupled simulation of a fusion line has been completed and shows grain structure formation very similar to the grain structure experimentally observed,
- Simulation results have shown that a decrease of the grain size and of the aspect ratio is possible by reducing the laser power at constant speed, or by increasing the travel speed at constant power. These results indicate the ability of our model to capture the effect of the process parameters on the grain structure in 316 L parts.

Moreover, current investigations on the adaptability of the present approach and model on describing solidification of powder-based configurations for AM applications are underway.

CRediT authorship contribution statement

Anaïs Baumard: Methodology, Software, Formal analysis, Investigation, Resources, Data curation, Writing - original draft, Writing - review & editing, Visualization. **Danièle Ayrault**: Supervision, Resources. **Olivier Fandeur**: Methodology, Software, Data curation. **Cyril Bordreuil**: Conceptualization, Methodology, Software, Investigation, Writing - original draft, Supervision, Project administration. **Frédéric Deschaux-Beaume**: Conceptualization, Formal analysis, Writing - original draft, Writing - review & editing, Visualization.

Declaration of Competing Interest

The authors declare that they have no known competing financial interests or personal relationships that could have appeared to influence the work reported in this paper.

Acknowledgments

The authors express their gratitude to the Processes and Engineering in Mechanics and Materials laboratory (PIMM - ENSAM) for carrying out the LPBF experiments.

Appendix A. Supplementary data

Supplementary data to this article can be found online at https://doi.org/10.1016/j.matdes.2020.109434.

References

[1] EPMA, Introduction to Additive Manufacturing Technology, 3rd ed., 2019.
[2] M. Revilla-León, I.M. Klemm, J. García-Arranz, M. Özcan, 3D metal printing - additive manufacturing technologies for frameworks of implant-borne fixed dental prosthesis, Eur. J. Prosthodont. Restor. Dent. 43 (2017) 143–147.
[3] A.A. Shapiro, J.P. Borgonia, Q.N. Chen, R.P. Dillon, B. Mc Enerney, R. Polit-Casillas, L. Soloway, Additive manufacturing for aerospace flight applications, J. Spacecr. Rocket. 53 (5) (2016)https://doi.org/10.2514/1.A33544.
[4] W.J. Sames, F.A. List, S. Pannala, R.R. Dehoff, S.S. Babu, The metallurgy and processing science of metal additive manufacturing, Int. Mater. Rev. 61–65 (2016) 315–360.
[5] O. Andreau, I. Koutiri, P. Peyre, J.D. Penot, N. Saintier, E. Pessard, T. De Terris, C. Dupuy, T. Baudin, Texture control of 316L parts by modulation of the melt pool morphology in selective laser melting, J. Mater. Process. Technol. 264 (2019) 21–31.
[6] D. Kong, X. Ni, C. Dong, L. Zhang, C. Man, X. Cheng, X. Li, Anisotropy in the microstructure and mechanical property for the bulk and porous 316L stainless steel fabricated via selective laser melting, Mater. Lett. 235 (2019) 1–5.
[7] K. Saeidi, X. Gao, Y. Zhong, Z.J. Shen, Hardened austenite steel with columnar subgrain structure formed by laser melting, Mater. Sci. Eng. A 625 (2015) 221–229.
[8] U. Scipioni Bertoli, B.E. MacDonald, J.M. Schoenung, Stability of cellular microstructure in laser powder bed fusion of 316L stainless steel, Mater. Sci. Eng. A 739 (2019) 109–117.
[9] Y. Zhong, L. Liu, S. Wikman, D. Cui, Z. Shen, Intragranular cellular segregation network structure strengthening 316L stainless steel prepared by selective laser melting, J. Nucl. Mater. 470 (2016) 170–178.
[10] J.A. Cherry, H.M. Davies, S.G.R. Brown, S. Mehmood, N.P. Lavery, J. Sienz, Investigation into the effect of process parameters on microstructural and physical properties of 316L stainless steel parts by selective laser melting, Int. J. Adv. Manuf. Technol. 76 (2015) 869–879.
[11] J.J.S. Dilip, B. Stucker, T.L. Starr, Effect of Process Parameters and Heat Treatment on the Microstructure and Mechanical Properties of SLM-Built HY100 Steel, Solid Freeform Fabrication Symposium, Austin, USA, 2014.
[12] T. Kurzynowski, E. Chlebus, B. Kuźnicka, J. Reiner, Parameters in Selective Laser Melting for processing metallic powders, SPIE 8239, High Power Laser Materials Processing: Lasers, Beam Delivery, Diagnostics, and Applications, San Francisco, USA, 2012.
[13] E. Liverani, S. Toschi, L. Ceschini, A. Fortunato, Effect of selective laser melting (SLM) process parameters on microstructure and mechanical properties of 316L austenitic stainless steel, J. Mater. Process. Technol. 249 (2017) 255–263.
[14] D. Sun, X. Li, W. Tan, A parametric study on grain structure in selective laser melting process for stainless steel 316L, Solid Freeform Fabrication Symposium, Austin, USA, 2017.
[15] B. Abstetar, SLM Processing-Microstructure-Mechanical Property Correlation in an Aluminum Alloy Produced by Additive Manufacturing, Graduate Theses 110 Montana Tech, 2016.
[16] J.P. Kruth, M. Badrossamay, E. Yasa, J. Deckers, L. Thijs, J. Van Humbeeck, Part and material properties in selective laser melting of metals, 16th International Symposium on Electromachining (ISEM XVI), Shanghai, 2010.
[17] D. Wang, C. Song, Y. Yang, Y. Bai, Investigation of crystal growth mechanism during selective laser melting and mechanical property characterization of 316L stainless steel parts, Mater. Des. 100 (2016) 291–299.
[18] K. Kunze, T. Etter, J. Grässlin, V. Shklover, Texture, anisotropy in microstructure and mechanical properties of IN738LC alloy processed by selective laser melting (SLM), Mater. Sci. Eng. A 620 (2015) 213–222.
[19] Y. Yang, Y. Zhu, M.M. Khonsari, H. Yang, Wear anisotropy of selective laser melted 316L stainless steel, Wear 428–429 (2019) 376–386.
[20] Y. Yang, X. Li, M.M. Khonsari, Y. Zhu, H. Yang, On enhancing surface wear resistance via rotating grains during selective laser melting, Addit. Manufact. 36 (December 2020) 101583.
[21] O. Zinovieva, A. Zinoviev, Numerical analysis of the grain morphology and texture in 316L steel produced by selective laser melting. International Conference on Advanced Materials with Hierarchical Structure for new Technologies and Reliable Structures, AIP Confer. Proc. 2167 (1) (2019) 020407, https://doi.org/10.1063/1.5132274.
[22] A. Rai, M. Markl, C. Körner, A coupled cellular automaton–lattice Boltzmann model for grain structure simulation during additive manufacturing, Comput. Mater. Sci. 124 (2016) 37–48.
[23] J.V. Neumann, The general and logical theory of automata, Hixon Symposium, 1948.
[24] M. Rappaz, C.A. Gandin, Probabilistic modelling of microstructure formation in solidification processes, Acta Metall. Mater. 41 (2) (1993) 345–360.
[25] C.A. Gandin, M. Rappaz, A coupled finite element-cellular automaton model for the prediction of dendritic grain structures in solidification processes, Acta Metall. Mater. 42–47 (1994) 2233–2246.
[26] C. Herriott, Z. Li, N. Kouraytem, V. Tari, W. Tan, B. Anglin, A.D. Rollett, A.D. Spear, A multi-scale multi-physics modeling framework to predict spatial variation of properties in additive-manufactured metals, Model. Simul. Mater. Sci. Eng. (2019) 27–32.
[27] Y. Lian, S. Lin, W. Yan, W.K. Liu, G.J. Wagner, A parallelized three-dimensional cellular automaton model for grain growth during additive manufacturing, Comput. Mech. 61 (2018) 543–558.
[28] Y. Lian, Z. Gan, C. Yu, D. Kats, W.K. Liu, G.J. Wagner, A cellular automaton finite volume method for microstructure evolution during additive manufacturing, Mater. Des. 169 (2019).
[29] X. Li, W. Tan, Numerical investigation of effects of nucleation mechanisms on grain structure in metal additive manufacturing, Comput. Mater. Sci. 153 (2018) 159–169.
[30] R.P. Shi, S. Khairallah, T. Roehling, T.W. Heo, J. McKeown, M.J. Matthews, Microstructural control in metal laser powder bed fusion additive manufacturing using beam shaping, Acta Mater. 184 (2020) 284–305.
[31] O. Zinovieva, A. Zinoviev, V. Ploshikhin, Three-dimensional modeling of the microstructure evolution during metal additive manufacturing, Comput. Mater. Sci. 141 (2018) 207–220.
[32] J.A. Koepf, M.R. Gotterbarm, M. Markl, C. Körner, 3D multi-layer grain structure simulation of powder bed fusion additive manufacturing, Acta Mater. 152 (2018) 119–126.
[33] W. Kurz, D.J. Fisher, Fundamentals of Solidification, Trans Tech Publication, 1984.
[34] W. Kurz, B. Giavanola, R. Trivedi, Theory of microstructural development during rapid solidification, Acta Metall. 34–35 (1986) 823–830.
[35] Cast3M, http://www-cast3m.cea.fr 2019.
[36] J. Goldak, A. Chakravarti, M. Bibby, A new finite element model for welding heat sources, Metall. Trans. B 15B (1984) 299–305.
[37] L. Depradeux, Simulation numérique du soudage-acier 316L: validation sur cas tests de complexité croissante, PhD Thesis; Villeurbanne, INSA 2004.
[38] S. Wolfram, Theory and Applications of Cellular Automata: Including Selected Papers 1983–1986, 1986.
[39] F. Aurenhammer, Voronoi diagrams – A survey of a fundamental geometric data structure, ACM Comput. Surv. 23 (3) (1991)https://doi.org/10.1145/116873.116880.

[40] C.A. Gandin, J.L. Desbiolles, M. Rappaz, P. Thevoz, A three-dimensional cellular automaton-finite element model for the prediction of solidification grain structures, Metal. Mater. Trans. A 30 (1999) 3153–3165.
[41] Dantzig and Rappaz, Solidification. , EPFL Presse, 2009.
[42] W. Tan, Y.C. Shin, Multi-scale modeling of solidification and microstructure development in laser keyhole welding process for austenitic stainless steel, Comput. Mater. Sci. 98 (2015) 446–458.
[43] H.J. Bunge, P.R. Morris, Texture Analysis in Materials Science - Mathematical Methods, Butterworth, London, 1982.
[44] C.A. Gandin, M. Rappaz, A 3D cellular automaton algorithm for the prediction of dendritic grain growth, Acta Mater. 45–55 (1997) 2187–2195.
[45] J. Lipton, W. Kurz, R. Trivedi, Rapid dendrite growth in undercooled alloys, Acta Metall. 35–44 (1987) 957–964.
[46] C. Mutke, K. Geenen, A. Röttger, W. Theisen, Interaction between laser radiation and metallic powder of 316L austenitic steel during selective laser melting, Mater. Charact. 145 (2018) 337–346.